Vapor deposited $n = 2$ Ruddlesden Popper interface layers aid charge carrier extraction in perovskite solar cells

Carlo A.R. Perini, [1] Andres Felipe Castro Mendez, [1] Tim Kodalle, [2] Magdalena Ravello, [1] Juanita Hidalgo, [1] Ruipeng Li, [3] Margherita Taddei, [4] Rajiv Giridharagopal, [4] Justin Pothoof, [4] Carolin M. Sutter-Fella, [2] David S. Ginger, [4] Juan-Pablo Correa-Baena[1*]

[1]School of Materials Science and Engineering, Georgia Institute of Technology, North Ave NW, Atlanta, Georgia 30332, USA

[2]Molecular Foundry, Lawrence Berkeley National Laboratory, 1 Cyclotron Road, Berkeley, California 94720, USA

[3]National Synchrotron Light Source II (NSLS-II), Brookhaven National Laboratory, Upton, New York, United States

[4]Department of Chemistry, University of Washington, Seattle, WA 98195-1700, USA.

Corresponding author: JPCB jpcorrea@gatech.edu

Abstract

Interfacial passivation with large organic cations such as phenetylammonium iodide has enabled superior performance for metal halide perovskite optoelectronic devices. However, the homogeneity of these interfaces and their formation dynamics are poorly understood. We study how Ruddlesden-Popper 2D phases form at a 3D perovskite interface when the 2D precursors are introduced via solution or via vapor. When using vapor deposition, we observe uniform coverage of the capping layer and the formation of a predominantly $n = 2$ Ruddlesden-Popper phase. In contrast, when using solution deposition, we observe presence of a mix of $n = 2$ and $n = 1$ in the film, and the formation of aggregates of the organic cations. As a result of the better phase purity and uniformity, vapor deposition enables higher median solar cell performance with narrower distribution compared to solution-treated films. This study provides fundamental information that the perovskite community can use to better design capping layers to achieve higher charge extraction efficiencies.

Introduction

The treatment of metal halide perovskite (MHP) interfaces with large organic cations have produced to date the highest performing devices for both MHP photovoltaics and light emission, but the understanding of the uniformity, formation, and carrier transport dynamics in these capping layers remains incomplete.[1–6] Upon treatment with bulky organic cations (too large to fit into the 3D MHP lattice) the surface of the 3D perovskite films evolves into lower dimensionality structures.[5] The formation of the capping layer and its crystal structure are affected by the organic cation used.[7] Many high performing solar cells presently rely on a Ruddlesden-Popper (RP) phase made at the interface, of formula $A'_2A_{n-1}B_nX_{3n+1}$, where A' is a bulky organic cation, A is an organic or inorganic cation (typically methylammonium, formamidinium, or cesium), B is a divalent cation (most commonly Pb), X is a halide anion (I, Br, Cl), and n indicates the number of planes of corner-sharing octahedra spaced by the bulky A' cations.[3,4,8] The RP phase can be formed by reconstructing the ABX_3 lattice typical of 3D perovskites. The crystallinity, the n number that characterizes the capping layer, and the coverage uniformity, affect the carrier transport properties.[6,8–13] However, it is not yet well understood which property have a larger impact on charge carrier transport, or whether a single n phase or a mix of phases with different n would be more beneficial.[6,8–13] Furthermore, the poor understanding of the mechanism of the interfacial layers' growth is a challenge to efforts to translate lab-scale device efficiencies to large area production.[6,8–13]

The deposition of bulky organic cations for interface passivation is predominantly carried out from solution.[9,14–16] Solvents have shown to play an important role in the formation of the 2D/3D interface and in its reconstruction from high n to low n RP phases.[6,9] Solvents as isopropanol (IPA) can dissolve the native A-site cations at the surface of the 3D film, making it PbI_2-rich and prone to convert to a RP phase, and favoring intermixing of 3D and 2D phases to aid charge extraction.[13,14] Owing to this complex interplay of effects, a clear understanding of the mechanisms that lead to the transformation of the 3D perovskite surface into phases of lower dimensionality

is still missing. However, we do know that the charge extraction is strongly dependent on the 2D layer thickness. Yet the control of thickness and uniformity via solution deposition methods is limited, particularly when low boiling point solvents such as IPA are used. [1,15,17,18] The thickness variance is even more detrimental when scaling to larger area devices.[19] As a result of the limited control enabled by solution deposition routes, significant differences in structure and performance have been reported by different groups.[1,5,8,9,15,17,18,20,21]

Vapor based routes present a promising alternative to solution deposition of the 2D interface films, as they enable superior uniformity, thickness, and composition control, while preventing solvent-mediated damage of the interface.[15,19,22] To date however, vacuum deposition of interface passivation films remains largely unexplored. A clear enhancement of solar cell efficiency has not yet been shown for vapor deposited organic cations.[15,22] Furthermore the performance of interface passivation layers deposited on the same solar cell processed via solution and vapor methods has not yet been investigated, making it difficult to understand whether the limitations observed via vapor treatment were intrinsic to the deposition route chosen, or related to the specific device architecture used.

In this work we investigate the formation dynamics of RP capping layers deposited via solution or via thermal evaporation before and after an annealing step. We perform Scanning Electron Microscopy (SEM), Grazing Incidence Wide-Angle X-ray Scattering (GIWAXS), and X-ray Photoelectron Spectroscopy (XPS) to study the morphology, structure, and composition of the interface modified with bulky cations, before and after annealing. We collect photoluminescence (PL) maps of the films with spatial and wavelength resolution to retrieve information about the uniformity of the optical properties of the films, corroborating our interpretations with Photoconductive Atomic Force Microscope maps (pc-AFM). Finally, we test the photovoltaic performances of the surface-modified films incorporated in complete solar cell stacks of structure Fluorine-doped thin oxide (FTO) | compact titanium dioxide (c-TiO_2) | mesoporous titanium dioxide (mp-TiO_2) | perovskite | phenethylammonium iodide (PEAI) | 2,2′,7,7′-tetrakis(N,N-di-p-methoxyphenyl-amine)9,9′-spirobifluorene (spiro-OMeTAD) | Au, shown in **Figure 1a**. By comparing capping layers deposited via solution and via vapor we demonstrate higher uniformity, improved open-circuit voltages (V_{OC}), and a preference to form $n = 2$ RP interfaces with less secondary phases in vapor deposited films. We observe that deposition from solvents such as IPA produces a mix of $n = 2$ and $n = 1$ phases at the surface of the films, either by progressive dimensional reduction or induced by variations in concentration of the bulky cations at the surface, as it has been suggested in previous reports. [6,9] Via vapor deposition of the capping layer we achieve the highest median power conversion efficiency (PCE). Our work demonstrates the potential of vapor deposition for interface passivation of MHP devices, a route to selectively form a $n = 2$ capping layer, and it provides fundamental insights towards the development of more efficient and reliable perovskite solar cells.

Results and Discussion

We use a triple cation, double halide 3D metal halide perovskite of nominal composition in solution $Cs_{0.06}MA_{0.16}FA_{0.79}PbI_{2.52}Br_{0.49}$, named here CsFAMA, as a benchmark to study how the interface of bulky-cation-treated 3D perovskites transforms into 2D RP phases. We select this composition due to its popularity in 3D/2D perovskite literature and its interfacial variations upon exposure to phenetylammonium iodide (PEAI).[5,6,15,20,23] We deposit PEAI via solution (labeled PEAI sol) on a CsFAMA perovskite surface using a concentration of 5 mg ml^{-1} in IPA. We deposit PEAI via vapor (PEAI vap) using thermal evaporation. A calibrated quartz crystal microbalance is used to regulate the deposition to a nominal amount of 10 nm. We note that the thickness of the PEAI layer deposited via vapor on the 3D MHP could vary from the nominal value for very thin films, as the sticking factor of the molecule changes depending on which material PEAI is deposited on and based on the exact composition and stoichiometry of the perovskite film. The schematic of the experiment is presented in **Figure 1a**. All films are studied before (PEAI sol 0, PEAI vap 0) and after a 10 min annealing at 100 °C (PEAI sol 10, PEAI vap 10), to provide thermal energy for the conversion of the interface into the RP phases.[5]

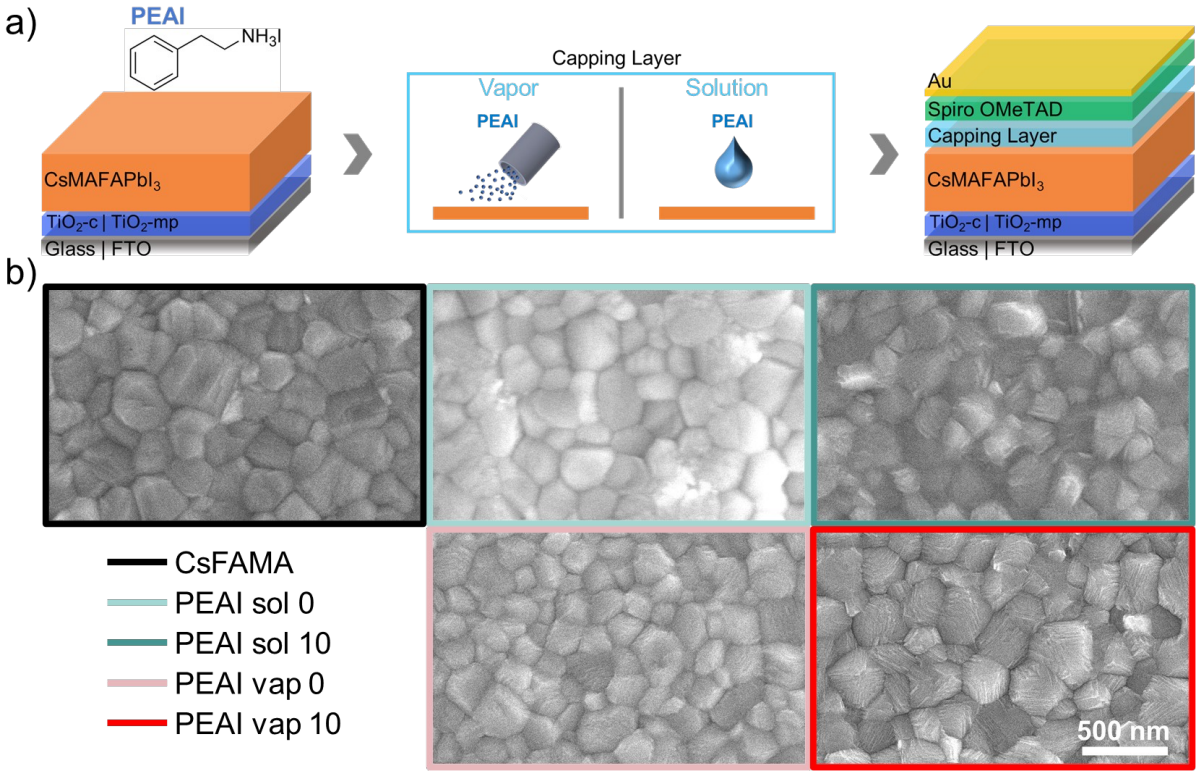

Figure 1. **Vapor and solution treatment of the perovskite interface.** (a) Schematics of the experiment. PEAI is deposited on the surface of a CsFAMA film via solution or via vapor. (b) SEM images of a pristine CsFAMA film (CsFAMA), of a solution treated film before (PEAI sol 0) and after (PEAI sol 10) a 10 min annealing

at 100 °C, and of a vapor deposited PEAI film before (PEAI vap 0) and after (PEAI vap 10) annealing.

Structure of the capping layer

We begin our study by comparing the microstructure of the solution and vapor treated films to the CsFAMA reference with SEM, presented in **Figure 1b**. Insulating organic molecules on the thin film surface, such as PEAI, tend to electrically charge when exposed to the SEM electron flow.[24] We relate charging in the image to the presence of the unreacted species or of a poorly conductive interlayer. In the reference CsFAMA film the grain boundaries are visible and the grain surfaces appear smooth. We observe a large charging effect in PEA sol 0 films, likely induced by the formation of an amorphous or RP layer at the surface, and bright agglomerates appear, which we ascribe to PEAI. Upon annealing in PEAI sol 10, we notice the disappearance of the bright aggregates and formation of crystal terraces and ledges at the surface of the grains. We relate less prominent grain boundaries in the PEAI sol 10 films after annealing, with the conversion of unreacted PEAI into a RP overlayer. In PEAI vap 0 films we see well defined crystal terraces and ledges right after deposition and no bright agglomerates. The grain boundaries are also clearly visible, marking either a thinner, or a more conformal layer on the grains surface. After annealing, in PEAI vap 10 films, we notice more defined terraces and ledges, minimized charging, and more visible grain boundaries. We ascribe these changes to increased crystallinity, as discussed below. The difference in SEM between vapor and solution deposition routes points at larger heterogeneity of the coating in solution-cast films. Vapor deposition instead results in films more conformal to the surface of the CsFAMA layer, and prevents the formation of aggregates of the bulky cations. Small variations in grain sizes are visible between films. However, the changes in size observed remain below the sample-to-sample experimental variability in CsFAMA films, and are not to be ascribed to the different interface treatments route used.

To investigate the formation of RP phases at the interface we performed GIWAXS on the films. The GIWAXS images of solution and vapor treated films are shown in **Figure S1**. All the low dimensional phases in **Figure S1** show preferential orientation of the (00*l*) planes parallel to the substrate (diffraction peaks at $q_r = 0$). Therefore, to maximize the signal from the 2D phases, we present in **Figure 2a** the sector averages around the q_z axis (vertical), retrieved from integration at an angle of ±20° around the axis. As show in **Figure 2a**, the solution processed films show diffraction peaks at a q of 0.28 $Å^{-1}$ and 0.36 $Å^{-1}$, attributed to the 001 plane of the $n = 2$ and the 002 plane of $n = 1$ RP phases, respectively.[25,26] Instead, the diffraction from the vapor treated layers shows a dominant $n = 2$ peak, with a $n = 1$ tail of significantly reduced intensity. Annealing of the films results in an increase of the diffraction intensity of the RP phases, but does not shift significantly the peak area ratio balance between the $n = 1$ and $n = 2$ phases (**Figure S2a**). In solution cast films, annealing of the layer drives further orientation with RP (00*l*) planes parallel to the substrate, which is not observed in vapor cast films (**Figure S2b**). The difference is in line with the observed changes in SEM. The PEAI sol 10 film microstructure shows the formation of layer on top of the MHP film that does not

fully follow the underlying MHP microstructure, while the PEAI vap 10 creates a conformal coating on the substrate, which likely imposes the spread in orientation observed for the 001 plane diffraction. We attribute the increased diffraction intensity from RP phases with annealing to the conversion of unreacted non crystalline PEAI at the surface and to a crystallization of amorphous phases at the interface. No clear vertical phase separation between $n = 1$ and $n = 2$ phases is observed, as shown by GIWAXS above and below the critical angle in **Figure S2a**.

In a previous work from Sargent's group it has been proposed that 3D perovskite films treated with bulky cations undergo transformation to RP via progressive dimensional reduction: the cations initially form $n > 1$ RP phases, to then convert into the $n = 1$ RP phase.[9] The presence of polar solvents that can solvate A-site cations in the ABX_3 3D perovskite structure, such as IPA, have been associated to a more rapid transformation to the $n = 1$ configuration.[6,9] Furthermore, the speed and type of conversion has also proven to be dependent on the perovskite composition used and on the concentration of the bulky cation in solution.[6] In this work we use a triple cation composition with double halide, on which we perform a static spin coat of the PEAI cation. The different composition, the shorter load time (we use 3-5 s), as well as the formation of bulky cation aggregates upon deposition via solution in **Figure 1b** could explain the presence both of $n = 1$ and $n = 2$ in our films after deposition, instead of a phase pure $n = 1$. Analogously, the absence of solvents during vapor deposition could be related to the higher $n = 2$ phase purity we observed. We corroborate these hypotheses by washing the surface of CsFAMA films with IPA before depositing PEAI via thermal evaporation and measuring GIWAXS on the films, which screens out any impact of surface composition on the formation of the different n phases (**Figure S1, S2c**).

While GIWAXS is an effective measure of the formation of crystalline phases at the interface, it is not accurate for the determination of the chemical composition of RP phases at the surface. We therefore use XPS to gather information on the average composition of the surface after the treatments. The N 1s and Pb 4f elemental scans of the pristine and treated films are presented in **Figure 2b** and **2c**, respectively. The elemental scans for the other relevant elements, namely Cs 3d, I 3d, O 1s, C 1s, and Br 3d, are presented in **Figure S3**, while the composition of the film at the surface, normalized to Pb is presented in **Table S1**. Both films with solution and thermally evaporated PEAI show attenuated signals for Cs, FA (C=N at 400.5 eV), I, and Pb with respect to the untreated reference, as shown in **Figure 2b, 2c**, and **Figure S3**. In the N 1s elemental scan in **Figure 2b**, the appearance of a peak at 402 eV is the C-N signature of the deposition of the PEA cation on the top surface of the perovskite layer.[5] The signals from Cs, FA, I, Pb are more attenuated in the sample where PEAI is deposited via solution, which could be ascribed to a thicker film being formed in the solution case or to unreacted PEAX (with X being I, Br) being left at the surface. When the films are annealed for 10 min at 100 °C to promote conversion of the surface layer to RP phases, the vapor deposited film shows a larger increase in FA with respect to its solution processed counterparts. The amounts of Pb and I increase comparably in both solution and vapor cast films, remaining higher in the vapor deposited samples. These changes would be

expected for the conversion to RP phases at the interface induced by annealing but could also stem from a loss of coverage of the PEAI film. The larger presence of FA and Pb at the surface of the vapor deposited film could also be related to the formation of phases with higher *n* observed when the deposition is carried out in absence of solvents. Based on the GIWAXS measurements and on the PL maps presented below we attribute the change in stoichiometry to the formation of a phase with higher *n* in the vapor treated films. We note that the halide stoichiometry at the surface is also changing. The amount of Br increases for all PEAI treated samples with respect to the untreated films (**Figure S3**, **Table S1**), which is counterintuitive with the addition of an iodide organic cation. We attribute the increase in Br and FA at the surface to the preference for PEAI or PEAI-based RP to incorporate available FA and Br from the 3D films.

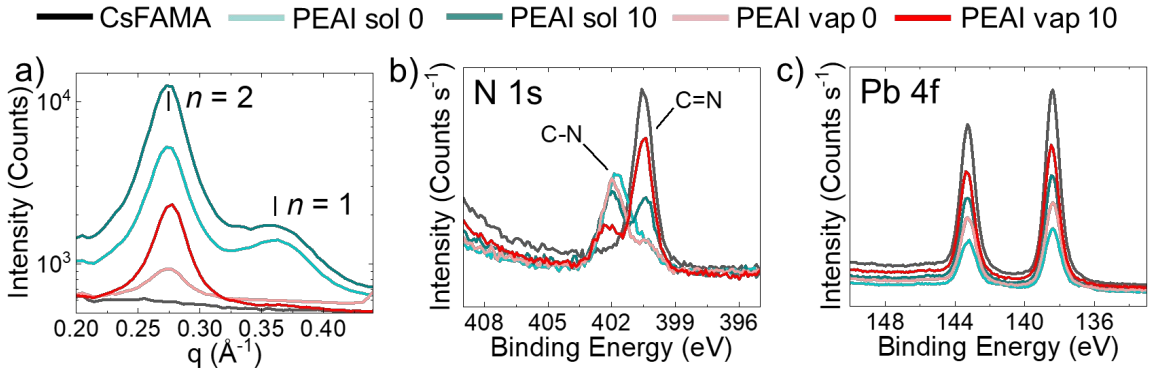

Figure 2. Surface structure induced by solution and thermal evaporation of bulky cations. (a) Sector average at ±20° azimuthal angle of the GIWAXS diffraction pattern of CsFAMA films with and without PEAI via solution and via vapor. XPS elemental scans of N 1s (b) and Pb 4f (c) of the films.

Optoelectronic performances

Next, we use hyperspectral PL microscopy and pc-AFM to investigate the optoelectronic heterogeneity and distribution of RP phases in the films as a function of the deposition method. Hyperspectral PL microscopy provides wavelength-resolved PL maps with a spectral resolution of ~2 nm and diffraction-limited spatial resolution. The PL of the pure 2D $n = 1$ and $n = 2$ have been previously characterized and they emit in the wavelength region of 500-515 nm and 540-560 nm, respectively.[18] The PL wavelength of pure CsFAMA lies at higher values, between 780 and 800 nm. We collected two hyperspectral PL maps, one in the emission region of the 2D phases (500-600 nm) and one of the 3D (600-900 nm). We can calculate the average PL spectra of the entire scanned regions by extracting the PL spectrum of every pixel and averaging for all the 1024 x 1024 pixels. In **Figure S4** we show the PL spatial maps of the CsFAMA sample, recorded at 505 nm, 550 nm, and 778 nm, which are representative of the luminescence distribution of $n = 1$, $n = 2$, and 3D, respectively. In **Figure S4a, b** we do not see any PL signal in the 2D region, as we expect for the reference CsFAMA films. **Figure S4c** shows emission from the 3D region. In **Figure S4d, e** we show the integrated PL spectra extracted from hyperspectral PL images in the 2D and 3D regions.

We compare the PL maps of the 2D phases after PEAI deposition. In **Figure 3 a-d** we show the spatial distribution of the $n = 2$ phase with PL emission at 550 nm across films treated with PEAI via solution (**Figure 3a, b**) and vapor (**Figure 3c, d**), before and after annealing. **Figure 3a** shows negligible PL from $n = 2$ for PEAI deposited via solution before annealing. The PL increases after annealing (**Figure 3b**) and for vapor deposition (**Figure 3c, d**). The PL from the films treated via vapor in **Figure 3 c, d** appears more heterogeneous than the PL from the solution coated layers, showing brighter areas on a less emissive background. However, the PL from $n = 2$ remains higher than 0 even in the least emissive areas, confirming full coverage of the $n = 2$ capping layer. Hyperspectral images of the $n = 1$ and 3D phases are shown in **Figure S5** and **S6**, respectively. **Figure 3e** shows the average PL spectra extracted from integration of the 2D hyperspectral maps. We observe predominant emission from the $n = 2$ phase in vapor-treated films, particularly after annealing, and mixed emission from both $n = 1$ and $n = 2$ phases in solution-treated films. The emission of the $n = 1$ phase at 505 nm is higher than the $n = 2$ emission for the annealed solution treated film. The $n = 1$ and $n = 2$ relative PL intensity mirrors what we see structurally with GIWAXS. The PL spectra of the 3D phases are shown in **Figure S7**. The broadening of PL emission can be used as another indicator of disorder in the capping layer. We extract the value of full width half maximum (FWHM) of the $n = 2$ PL emission using a gaussian fit (fit details in **Table S1**). **Figure 3e** shows the fitting for the annealed solution treated sample and the ones treated via vapor deposition. The vapor annealed sample shows the smallest FWHM of 21 nm which is consistent with improved uniformity of the $n = 2$ phase. Overall, the hyperspectral PL maps show that vapor treated films have a more homogeneous and dominant $n = 2$ phase at the interface, which reduces electronic disorder and could enable better charge extraction. Best $n = 2$ uniformity is achieved combining vapor deposition and annealing of the capping layer.

We further analyzed 2D coverage performing pc-AFM measurements on the same area highlighted with a red square in **Figure 3a-d**. We can use the variations in the current density of passivated layers with respect to the reference as a probe for the presence of the bulky cations molecules on the film. In these data, we observe current heterogeneity in all of the treated films, though as presented in the plot in **Figure S8**, all passivated samples exhibit currents significantly lower than those in the unpassivated (3D) film, which is expected if there is full coverage of the underlying layer both via vapor and via solution. Heterogeneity is observed in all treated films even at higher magnifications, as shown by the 3 μm x 3 μm pc-AFM images (**Figure S9)**.

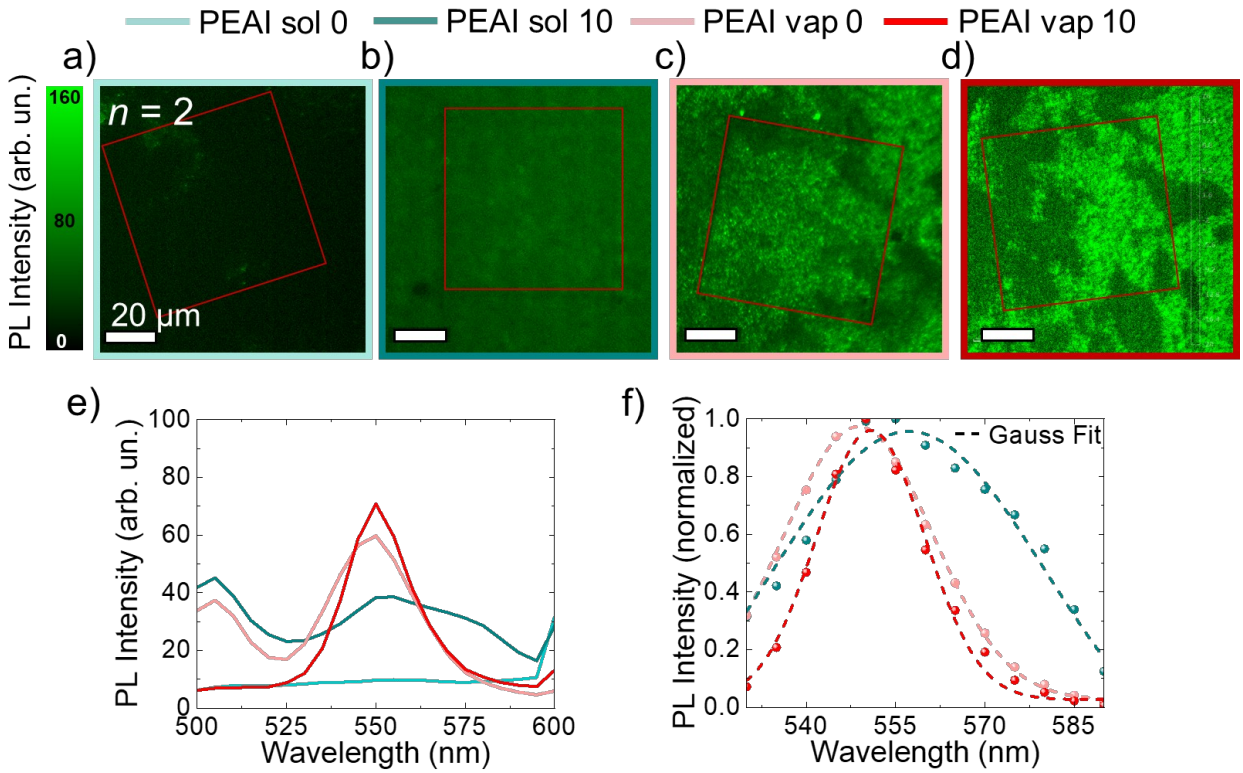

Figure 3. *n* = 2 photoluminescence of PEAI-treated CsFAMA films. (a-d) 80 µm x 80 µm hyperspectral photoluminescence maps at 550 nm for PEAI sol 0 (a), PEAI sol 10 (b), PEAI vap 0 (c), PEAI vap 10 (d). Square overlays in red indicate 60 µm x 60 µm regions used for pc-AFM. (e) Photoluminescence spectra extracted from hyperspectral PL maps recorded in the 2D emission region (500-600 nm). (f) PL spectra (solid lines) and Gaussian fit (dashed lines) of the *n* = 2 emission. To fit the PL, the spectra were normalized to 1 at their maximum, and zero in the minimum (considering the region 525-595 nm). The fit equation and parameters extracted are summarized in **Table S2**.

Having studied the morphological, structural, chemical, and optical properties of the films, we move to characterize the photovoltaic performances of a solar cell stack incorporating the modified layers. We use the device structure presented in **Figure 1a**, FTO | c-TiO_2 | mp-TiO_2 | CsFAMA | PEAI | spiro-OMeTAD | Au, with the PEAI layer being introduced via solution or vapor. We report the complete photovoltaic parameters of the cells in **Figure S10**. **Figure 4a, b** show the open circuit voltage (V_{OC}) extracted from the reverse current-voltage (*J-V*) scan of the devices and the stabilized power conversion efficiency (*PCE*) of the solar cells after being held at their maximum power point for 1 min. The *J-V* reverse scans for the champion devices of each variation are reported in **Figure S11**. In **Figure 4a, b** the reference CsFAMA shows a median V_{OC} of 1.11 V and a median stabilized PCE of 17.7 %. The vapor treated films (PEAI vap 0) show an improvement to 1.12 V of the median V_{OC} and a drop to 17 % of the PCE, suggesting reduced recombination but impaired charge extraction from the device. This is further supported by the reduction in short circuit current (J_{SC}) in **Figure S10**. For the solution deposited PEAI (PEAI sol 0) the median V_{OC} decreases to 1.10 V, but the average PCE increases to

18.3 %. The drop in V_{OC} observed upon introduction of PEAI via solution is caused by defects induced by IPA when PEAI is deposited on the CsFAMA film via solution, as confirmed by the V_{OC} of control films in **Figure S12** where the surface of CsFAMA was washed with IPA. The enhanced PCE correlates with improved Fill Factor (*FF*) in **Figure S10**. Annealing of the bulky cation layer heals the defects in the solution-treated film. The V_{OC} of both solution and vapor treated films increases upon annealing, reaching a median V_{OC} of 1.13 V and peaking at 1.19 V in both cases. However, the vapor treated films produce the highest median stabilized PCE of 18.4 % and the narrowest PCE distribution among all variations, against the solution annealed films that decrease to a PCE of 17.8 %. The variations in *stabilized PCE* observed between solution and vapor deposited films correlate with the higher n = 2 RP phase purity at the interface, suggesting that attaining a phase-pure RP passivation layer enables better charge extraction from the CsFAMA film while granting effective passivation of the surface of perovskite grains.

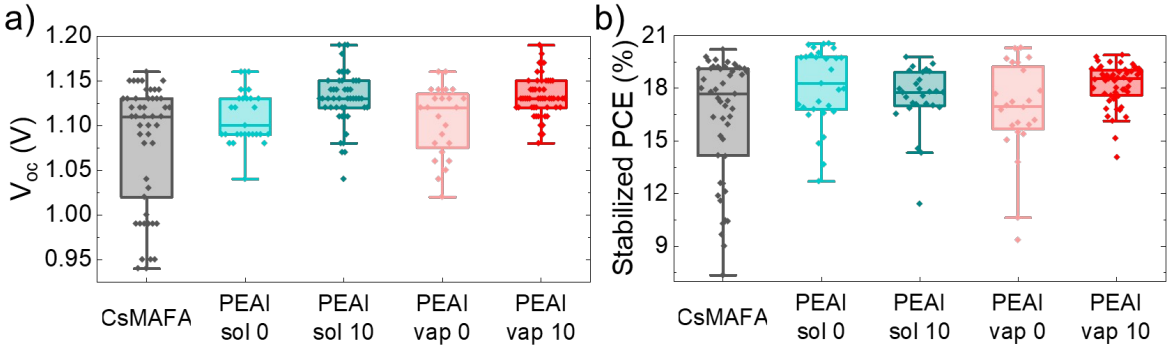

Figure 4 Photovoltaic performances. (a) V_{OC} distribution of solar cells, (b) *Stabilized PCE*, and maximum power point tracking of: CsFAMA - untreated 3D perovskite layer; PEAI sol 0 - 3D layer passivated with PEAI via solution and not annealed; PEAI sol 10 - 3D layer passivated with PEAI via solution and annealed for 10 min at 100 °C. PEAI vap 0 - 3D layer passivated with PEAI via thermal evaporation and not annealed. PEAI vap 10 - 3D layer passivated with PEAI via vapor and annealed for 10 min at 100 °C.

Conclusions

We have investigated the transformation of the 3D perovskite interface into Ruddlesden-Popper (RP) phases upon interaction with bulky cations deposited via solution or vapor. We showed that the use of a solvent like IPA induced formation of defects at the interface and formation of both n = 1 and n = 2 RP phases. Instead, the deposition of PEAI via thermal evaporation results in the formation of a RP interface dominantly composed of n = 2, avoiding solvent damage of the treated interface. The deposition of bulky cations via vapor enables the formation of more homogeneous films than in solution, which reduces the spread in power conversion efficiencies when the layers are incorporated in complete solar cell stacks. This is of relevance towards industrial application of the technology, both for reproducibility,

and for the easier scalability to large area of vacuum-based processes. Based on our observations, we propose vapor deposition as a more suitable tool than solution to enable control on the formation of capping layers based on RP phases. We believe that optimizing the treatment of the interface before the deposition of bulky cations via vapor, and the thickness deposited, represents the most promising route towards forming phase-pure and defined 3D | 2D interfaces, to enable higher performances and stability of interface-passivated metal halide perovskite solar cells.

Acknowledgements

C.A.R.P. thanks Robert Westbrook for the discussion of hyperspectral PL maps. C.A.R.P. and J.P. received financial support from the U.S. Department of Energy's Office of Energy Efficiency and Renewable Energy (EERE) under the Solar Energy Technologies Office Award Number DE40 EE0009369. T.K. thanks the German Research Foundation (DFG) for funding (fellowship number KO6414). M.T. acknowledge funding the Office of Naval Research (Award # N00014-20-1-2587) and U.S. Department of Energy's Office of Energy Efficiency and Renewable Energy (EERE) under the Solar Energy Technology Office (SETO), Award Number DE-EE0008747. This research used the CMS beamline of National Synchrotron Light Source II, a U.S. Department of Energy (DOE) Office of Science User Facility operated for the DOE Office of Science by Brookhaven National Laboratory under contract DE-SC0012704. The work was further supported by an Integrative Travel Fund sponsored through NSF award DMR-2019444. Work at the Molecular Foundry was supported by the Office of Science, Office of Basic Energy Sciences, of the U.S. Department of Energy under Contract No. DE-AC02-05CH11231. Part of the experimental work was carried out in the UW Clean Energy Institute Research Training Testbed facility. The Atomic force microscopy, and R.G.'s contribution to this work was supported by the DOE Office of Basic Energy Sciences, Division of Materials Sciences and Engineering under Award DOE-SC0013957. Part of this work was conducted with instrumentation at the Molecular Analysis Facility, a National Nanotechnology Coordinated Infrastructure site at the University of Washington, which is a user facility supported in part by the National Science Foundation (Grant ECC-1542101), the University of Washington, the Molecular Engineering & Sciences Institute, the Clean Energy Institute, and the National Institutes of Health. We acknowledge support by the State of Washington through the University of Washington Clean Energy Institute and the Washington Research Foundation.

References

(1) Perini, C. A. R.; Doherty, T. A. S.; Stranks, S. D.; Correa-Baena, J. P.; Hoye, R. L. Z. Pressing Challenges in Halide Perovskite Photovoltaics—from the Atomic to Module Level. *Joule* **2021**, *5* (5), 1024–1030. https://doi.org/10.1016/J.JOULE.2021.03.011.

(2) Xu, W.; Hu, Q. H.; Bai, S.; Bao, C.; Miao, Y.; Yuan, Z.; Borzda, T.; Barker, A. J.; Tyukalova, E.; Hu, Z. H.; Kawecki, M.; Wang, H.; Yan, Z.; Liu, X.; Shi, X. S.; Uvdal, K.; Fahlma, M.; Gao, F. Rational Molecular Passivation for High-Performance Perovskite

Light-Emitting Diodes. *Nat Photonics* **2019**, doi.org/10.1038/nphoton.2019.xxx. https://doi.org/10.1038/s41566-019-0390-x.

(3) Kim, M.; Jeong, J.; Lu, H.; Lee, T. K.; Eickemeyer, F. T.; Liu, Y.; Choi, I. W.; Choi, S. J.; Jo, Y.; Kim, H. B.; Mo, S. I.; Kim, Y. K.; Lee, H.; An, N. G.; Cho, S.; Tress, W. R.; Zakeeruddin, S. M.; Hagfeldt, A.; Kim, J. Y.; Grätzel, M.; Kim, D. S. Conformal Quantum Dot-SnO2 Layers as Electron Transporters for Efficient Perovskite Solar Cells. *Science (1979)* **2022**, *375* (6578), 302–306. https://doi.org/10.1126/science.abh1885.

(4) Yoo, J. J.; Seo, G.; Chua, M. R.; Park, T. G.; Lu, Y.; Rotermund, F.; Kim, Y.-K. K.; Moon, C. S.; Jeon, N. J.; Correa-Baena, J.-P. P.; Bulović, V.; Shin, S. S.; Bawendi, M. G.; Seo, J. Efficient Perovskite Solar Cells via Improved Carrier Management. *Nature* **2021**, *590* (7847), 587–593. https://doi.org/10.1038/s41586-021-03285-w.

(5) Perini, C. A. R.; Correa-Baena, J.; Rojas-Gatjens, E.; Ravello, M.; Felipe, A.; Mendez, C.; Hidalgo, J.; An, Y.; Li, R.; Silva-Acuña, C.; Correa-Baena, J.-P. Preventing Bulky Cation Diffusion in Lead Halide Perovskite Solar Cells. *Under review* **2021**. https://doi.org/10.33774/CHEMRXIV-2021-197PF.

(6) Kodalle, T.; Moral, R. F.; Scalon, L.; Szostak, R.; Abdelsamie, M.; Marchezi, P. E.; Nogueira, A. F.; Sutter-Fella, C. M. Revealing the Transient Formation Dynamics and Optoelectronic Properties of 2D Ruddlesden-Popper Phases on 3D Perovskites. *Adv Energy Mater* **2022**, 2201490. https://doi.org/10.1002/aenm.202201490.

(7) Li, X.; Hoffman, J. M.; Kanatzidis, M. G. The 2D Halide Perovskite Rulebook: How the Spacer Influences Everything from the Structure to Optoelectronic Device Efficiency. *Chem Rev* **2021**, *121* (4), 2230–2291. https://doi.org/10.1021/acs.chemrev.0c01006.

(8) Jang, Y. W.; Lee, S.; Yeom, K. M.; Jeong, K.; Choi, K.; Choi, M.; Noh, J. H. Intact 2D/3D Halide Junction Perovskite Solar Cells via Solid-Phase in-Plane Growth. *Nat Energy* **2021**, *6* (1), 63–71. https://doi.org/10.1038/s41560-020-00749-7.

(9) Proppe, A. H.; Johnston, A.; Teale, S.; Mahata, A.; Quintero-Bermudez, R.; Jung, E. H.; Grater, L.; Cui, T.; Filleter, T.; Kim, C. Y.; Kelley, S. O.; de Angelis, F.; Sargent, E. H. Multication Perovskite 2D/3D Interfaces Form via Progressive Dimensional Reduction. *Nat Commun* **2021**, *12* (1), 1–9. https://doi.org/10.1038/s41467-021-23616-9.

(10) Xi, J.; Byeon, J.; Kim, U.; Bang, K.; Han, G. R.; Kim, J.-Y.; Yoon, J.; Dong, H.; Wu, Z.; Divitini, G.; Xi, K.; Park, J.; Lee, T.-W.; Kim, S. K.; Choi, M.; Lee, J. W. Abnormal Spatial Heterogeneity Governing the Charge-Carrier Mechanism in Efficient Ruddlesden–Popper Perovskite Solar Cells. *Energy Environ Sci* **2021**, *14* (9), 4915–4925. https://doi.org/10.1039/D1EE00984B.

(11) Azmi, R.; Ugur, E.; Seitkhan, A.; Aljamaan, F.; Subbiah, A. S.; Liu, J.; Harrison, G. T.; Nugraha, M. I.; Eswaran, M. K.; Babics, M.; Chen, Y.; Xu, F.; Allen, T. G.; Rehman, A. ur; Wang, C.-L.; Anthopoulos, T. D.; Schwingenschlögl, U.; de Bastiani, M.; Aydin, E.; de Wolf, S. Damp Heat–Stable Perovskite Solar Cells with Tailored-Dimensionality

2D/3D Heterojunctions. *Science (1979)* **2022**, *376* (6588), 73–77. https://doi.org/10.1126/science.abm5784.

(12) Duong, T.; Pham, H.; Kho, T. C.; Phang, P.; Fong, K. C.; Yan, D.; Yin, Y.; Peng, J.; Mahmud, M. A.; Gharibzadeh, S.; Nejand, B. A.; Hossain, I. M.; Khan, M. R.; Mozaffari, N.; Wu, Y.; Shen, H.; Zheng, J.; Mai, H.; Liang, W.; Samundsett, C.; Stocks, M.; McIntosh, K.; Andersson, G. G.; Lemmer, U.; Richards, B. S.; Paetzold, U. W.; Ho-Ballie, A.; Liu, Y.; Macdonald, D.; Blakers, A.; Wong-Leung, J.; White, T.; Weber, K.; Catchpole, K. High Efficiency Perovskite-Silicon Tandem Solar Cells: Effect of Surface Coating versus Bulk Incorporation of 2D Perovskite. *Adv Energy Mater* **2020**, *10* (9), 1903553. https://doi.org/10.1002/aenm.201903553.

(13) Mahmud, M. A.; Duong, T.; Peng, J.; Wu, Y.; Shen, H.; Walter, D.; Nguyen, H. T.; Mozaffari, N.; Tabi, G. D.; Catchpole, K. R.; Weber, K. J.; White, T. P. Origin of Efficiency and Stability Enhancement in High-Performing Mixed Dimensional 2D-3D Perovskite Solar Cells: A Review. *Adv Funct Mater* **2022**, *32* (3), 2009164. https://doi.org/10.1002/adfm.202009164.

(14) Tan, S.; Huang, T.; Yavuz, I.; Wang, R.; Weber, M. H.; Zhao, Y.; Abdelsamie, M.; Liao, M. E.; Wang, H. C.; Huynh, K.; Wei, K. H.; Xue, J.; Babbe, F.; Goorsky, M. S.; Lee, J. W.; Sutter-Fella, C. M.; Yang, Y. Surface Reconstruction of Halide Perovskites during Post-Treatment. *J Am Chem Soc* **2021**, *143* (18), 6781–6786. https://doi.org/10.1021/jacs.1c00757.

(15) La-Placa, M. G.; Gil-Escrig, L.; Guo, D.; Palazon, F.; Savenije, T. J.; Sessolo, M.; Bolink, H. J. Vacuum-Deposited 2D/3D Perovskite Heterojunctions. *ACS Energy Lett* **2019**, *4* (12), 2893–2901. https://doi.org/10.1021/acsenergylett.9b02224.

(16) Jariwala, S.; Burke, S.; Dunfield, S.; Shallcross, R. C.; Taddei, M.; Wang, J.; Eperon, G. E.; Armstrong, N. R.; Berry, J. J.; Ginger, D. S. Reducing Surface Recombination Velocity of Methylammonium-Free Mixed-Cation Mixed-Halide Perovskites via Surface Passivation. *Chemistry of Materials* **2021**, *33* (13), 5035–5044. https://doi.org/10.1021/acs.chemmater.1c00848.

(17) Jiang, Q.; Zhao, Y.; Zhang, X.; Yang, X.; Chen, Y.; Chu, Z.; Ye, Q.; Li, X.; Yin, Z.; You, J. Surface Passivation of Perovskite Film for Efficient Solar Cells. *Nat Photonics* **2019**, *13* (7), 460–466. https://doi.org/10.1038/s41566-019-0398-2.

(18) Sutanto, A. A.; Szostak, R.; Drigo, N.; Queloz, V. I. E.; Marchezi, P. E.; Germino, J. C.; Tolentino, H. C. N.; Nazeeruddin, M. K.; Nogueira, A. F.; Grancini, G. In Situ Analysis Reveals the Role of 2D Perovskite in Preventing Thermal-Induced Degradation in 2D/3D Perovskite Interfaces. *Nano Lett* **2020**, *20* (5), 3992–3998. https://doi.org/10.1021/acs.nanolett.0c01271.

(19) Ávila, J.; Momblona, C.; Boix, P. P.; Sessolo, M.; Bolink, H. J. Vapor-Deposited Perovskites: The Route to High-Performance Solar Cell Production? *Joule* **2017**, *1* (3), 431–442. https://doi.org/10.1016/j.joule.2017.07.014.

(20) Degani, M.; An, Q.; Albaladejo-Siguan, M.; Hofstetter, Y. J.; Cho, C.; Paulus, F.; Grancini, G.; Vaynzof, Y. 23.7% Efficient Inverted Perovskite Solar Cells by Dual

Interfacial Modification. *Sci Adv* **2021**, *7* (49), 7930. https://doi.org/10.1126/sciadv.abj7930.

(21) Teale, S.; Proppe, A. H.; Jung, E. H.; Johnston, A.; Parmar, D. H.; Chen, B.; Hou, Y.; Kelley, S. O.; Sargent, E. H. Dimensional Mixing Increases the Efficiency of 2D/3D Perovskite Solar Cells. *J Phys Chem Lett* **2020**, *11* (13), 5115–5119. https://doi.org/10.1021/acs.jpclett.0c01444.

(22) Lin, D.; Zhang, T.; Wang, J.; Long, M.; Xie, F.; Chen, J.; Wu, B.; Shi, T.; Yan, K.; Xie, W.; Liu, P.; Xu, J. Stable and Scalable 3D-2D Planar Heterojunction Perovskite Solar Cells via Vapor Deposition. *Nano Energy* **2019**, *59*, 619–625. https://doi.org/10.1016/j.nanoen.2019.03.014.

(23) Wang, J.; Jin, G.; Zhen, Q.; He, C.; Duan, Y. Bulk Passivation and Interfacial Passivation for Perovskite Solar Cells: Which One Is More Effective? *Adv Mater Interfaces* **2021**, *8* (9), 2002078. https://doi.org/10.1002/admi.202002078.

(24) Egerton, R. F.; Li, P.; Malac, M. Radiation Damage in the TEM and SEM. In *Micron*; 2004; Vol. 35, pp 399–409. https://doi.org/10.1016/j.micron.2004.02.003.

(25) Morrow, D. J.; Hautzinger, M. P.; Lafayette, D. P.; Scheeler, J. M.; Dang, L.; Leng, M.; Kohler, D. D.; Wheaton, A. M.; Fu, Y.; Guzei, I. A.; Tang, J.; Jin, S.; Wright, J. C. Disentangling Second Harmonic Generation from Multiphoton Photoluminescence in Halide Perovskites Using Multidimensional Harmonic Generation. *Journal of Physical Chemistry Letters* **2020**, *11* (16), 6551–6559. https://doi.org/10.1021/acs.jpclett.0c01720.

(26) Song, J.; Dang, Y.; Liu, X. L.; Tao, X. Layered Hybrid Lead Perovskite Single Crystals: Phase Transformations and Tunable Optical Properties. *CrystEngComm* **2020**, *22* (38), 6310–6315. https://doi.org/10.1039/d0ce00753f.